Gypsum Scale Formation and Inhibition Kinetics with Implications in Membrane System

Zhaoyi Dai [1, 2, 3,*], Yue Zhao [3, 4], Samridhdi Paudyal [3], Xin Wang [3], Chong Dai [3], Saebom Ko [3], Wei Li [3], Amy T. Kan [3], Mason B. Tomson [3]

[1] State Key Laboratory of Biogeology and Environmental Geology, School of Earth Sciences, China University of Geosciences, Wuhan 430074, China

[2] Hubei Key Laboratory of Critical Zone Evolution, School of Earth Sciences, China University of Geosciences, Wuhan 430074, China

[3] Department of Civil and Environmental Engineering, Rice University, 6100 Main Street, Houston, Texas 77005, United States

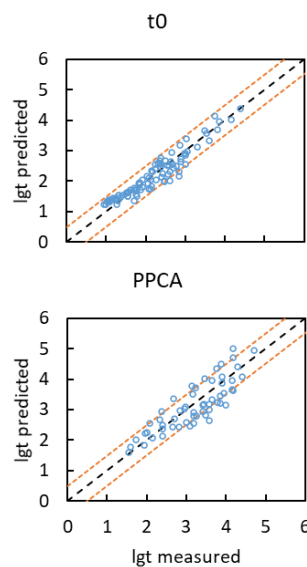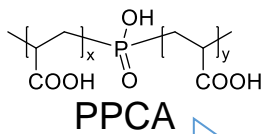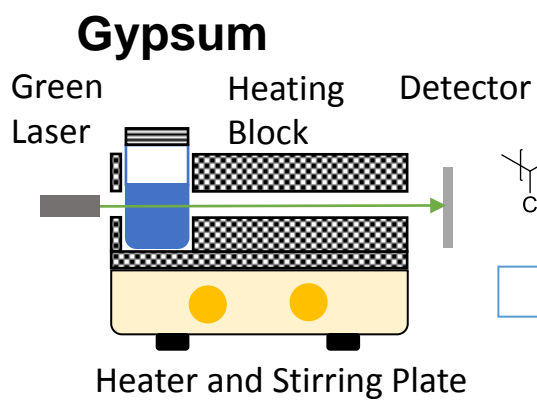[4] Research Institute of Petroleum Processing, SINOPEC, Beijing, China

* Corresponding author. Tel.: +86-13675620524, E-mail: dzy616@gmail.com

Abstract

Water desalination using membrane technology is one of the main technologies to resolve water pollution and scarcity issues. In the membrane treatment process, mineral scale deposition and fouling is a severe challenge that can lead to filtration efficiency decrease, permeate quality compromise, and even membrane damage. Multiple methods have been developed to resolve this problem, such as scale inhibitor addition, product recovery ratio adjustment, periodic membrane surface flushing. The performance of these methods largely depends on the ability to accurately predict the kinetics of mineral scale deposition and fouling with or without inhibitors. Gypsum is one of the most common and troublesome inorganic mineral scales in membrane systems, however, no mechanistic model is available to accurately predict the induction time of gypsum crystallization and inhibition. In this study, a new gypsum crystallization and inhibition model based on the classical nucleation theory and a Langmuir type adsorption isotherm has been developed. Through this model, it is believed that gypsum nucleation may gradually transit from homogeneous to heterogeneous nucleation when the gypsum saturation index (SI) decreases. Such transition is represented by a gradual decrease of surface tension at smaller SI. This model assumes that the adsorption of inhibitors onto the gypsum nucleus can increase the nucleus superficial surface tension and prolong the induction time. Using the new model, this study accurately predicted the gypsum crystallization induction times with or without nine commonly used scale inhibitors over wide ranges of temperature (25 – 90 °C), SI (0.04 – 0.96), and background NaCl concentration (0 – 6 mol/L). The fitted affinity constants between scale inhibitors and gypsum show a good correlation with those between the same inhibitors and barite, indicating a similar inhibition mechanism via adsorption. Furthermore, by incorporating this model with the two-phase mineral deposition model our group developed previously, this study accurately predicts the gypsum deposition time on the membrane material surfaces reported in the literature. We believe that the model developed in this study can not only accurately predict the gypsum crystallization induction time with or without scale inhibitors, elucidate the gypsum crystallization and inhibition mechanisms, but also optimize the mineral scale control in the membrane filtration system.

Keywords

33 **TOC**

Gypsum

Green   Heating   Detector
Laser   Block

Heater and Stirring Plate

PPCA

t0

PPCA

lgt predicted

lgt measured

34
35
36

1. Introduction

Water scarcity is becoming more severe due to the continuously growing population, developing economies, and increasing water pollutions (Dai and Li, 2013; Huang et al., 2020; Yu et al., 2019). Water desalination has been playing a more important role especially when cost continues to drop (Ghaffour et al., 2013; Huang et al., 2020). Ghaffour et al. (2013) reported that the membrane process accounts for 63.7% of the total global desalted water capacity. In membrane processes, the elevation of ion concentrations, the changes of temperature and pressure, and the occurrence of concentration polarization can lead to the mineral scale formation and fouling in the membrane system (Al-Roomi and Hussain, 2016; Lioliou et al., 2006; Warsinger et al., 2015; Yu et al., 2019). Such inorganic scale formation has become a major limiting factor of membrane system applications (Lin et al., 2005; Rabie et al., 2001; Seidel and Elimelech, 2002; Speth et al., 1998; Van der Bruggen et al., 2001). Specifically, it can decrease the permeation rate, increase the osmotic pressure, increase contaminant breakthrough and compromise permeate water quality, and cause membrane damage (Huang et al., 2020; Lin et al., 2005; Shirazi et al., 2010; Warsinger et al., 2015).

Gypsum ($CaSO_4 \cdot 2H_2O$, calcium sulfate dihydrate) is one of the most common inorganic mineral scales in membrane systems (Warsinger et al., 2015; Yu et al., 2019). Since gypsum is not acid soluble and is a tenacious and adherent scale on the membrane surfaces, it has become one of the most troublesome scale minerals (Gryta, 2009). To effectively control the gypsum scale problem, different strategies have been proposed to ensure the induction time is longer than the crystallization or deposition time in the membrane operation system using different techniques. For example, the cations (i.e., Ca^{2+}) and/or anions (i.e., SO_4^{2-}) can be selectively removed to decrease the saturation level of gypsum (and thus increase the induction time) by ion-exchange (Kelle Zeiher et al., 2003; Mukhopadhyay, 2003) or capacitive deionization process using composite electrodes (Zuo et al., 2018). Antony et al. (2011) suggested to limit the product recovery so that the saturation level of gypsum in the concentrate stream is controlled below a certain saturation level, which limited the economic efficiency of membrane system at the same time (Antony et al., 2011). It was also proposed to periodically flush membrane surface or reverse flow directions to shorten the time for crystallization and deposition less than the induction time (Lee et al., 2018; Nghiem and Cath, 2011; Pomerantz et al., 2006; Uchymiak et al., 2009; Warsinger et al., 2015). At the same time, various scale inhibitors (or antiscalants) have been widely used to prolong the induction time (Al-Roomi and Hussain, 2016; Antony et al., 2011; Lin and Singer, 2005; Lioliou et al., 2006; Rosenberg et al., 2012; Warsinger et al., 2015; Yu et al., 2019). Among all these methods above, the accurate prediction of the gypsum crystallization induction time is critical to achieve optimal efficiency.

The mineral induction time (t_{ind}) is defined as the time elapsed between the establishment of supersaturation and the detection of mineral formation (Mullin, 2001; Nielsen, 1964). This definition shows that the induction time has a significant practical meaning and it has been widely used to indicate when the damage starts to occur in different processes (He et al., 1996; Knezic et al., 2004; Mullin, 2001; Nielsen, 1964; Van der Leeden et al., 1992). In previous research, different

77   experimental methods were utilized to measure the gypsum induction time, including measuring
78   solution turbidity with a turbidity meter or a laser apparatus (He et al., 1994a, 1994b; Lancia et al.,
79   1999; Paudyal et al., 2020), measuring partial pressure change in a dynamic scale loop (Al-Roomi
80   and Hussain, 2016), or measuring the frequency change on a QCM (quartz crystal microbalance)
81   sensor (Alimi et al., 2003). Yan et al. (2015) and Zhang et al. (2017) have confirmed that the
82   induction time achieved by monitoring solution turbidity and partial pressure of tubing are
83   comparable with each other (Yan et al., 2015; Zhang et al., 2017). Using these experimental
84   apparatus, the induction time of gypsum crystallization without inhibitors (Alimi et al., 2003; He
85   et al., 1994a) and with various inhibitors (Al-Roomi and Hussain, 2016; Lioliou et al., 2006;
86   Paudyal et al., 2020; Prisciandaro et al., 2006; Rosenberg et al., 2012; Yu et al., 2019) have been
87   determined. Unfortunately, there is not a quantitative model available that can accurately predict
88   gypsum induction time with or without scale inhibitors at different operation conditions. He and
89   his colleagues developed semi-empirical models for the induction time prediction of calcite, barite,
90   and celestite with or without scale inhibitors (He et al., 1999, 1996, 1995a, 1995b, 1994b).
91   However, the induction times of gypsum does not show the similar trend with other minerals and
92   cannot be described by the semi-empirical models, probably due to the relatively larger solubility
93   and variable surface tension of gypsum at different saturation levels (He et al., 1994a). It was also
94   suggested that the fundamentals of inhibition mechanisms are not well understood with little
95   guidance from literature (Al-Roomi and Hussain, 2016). Therefore, in order to optimize the
96   gypsum scale control in the membrane system with the methods introduced above, a quantitative
97   model with solid theoretical basis is needed to accurately predict the gypsum crystallization
98   induction time with or without inhibitors.
99   In this study, a new model based on classical nucleation theory (CNT) with saturation index
100   (SI) dependent surface tension is developed to predict the induction time of gypsum crystallization.
101   This mechanistic model shows that the surface tension decreases when the gypsum crystallization
102   transits from homogeneous nucleation at relatively larger SI values to heterogeneous nucleation at
103   smaller SI values. A Langmuir-type adsorption model was adopted to quantify the impacts of scale
104   inhibitors. This new model assumes that the inhibition mechanism is dominated by the inhibitor
105   adsorption to the nucleus surface and the alternation of the effective surface tension, and can
106   accurately predict the gypsum crystallization induction time with or without nine commonly used
107   scale inhibitors over wide ranges of temperature (25 – 90 °C), SI (0.04 – 0.96), and background
108   NaCl concentration (0 – 6 mol/L). Such good agreement between the model predictions and the
109   experimental data supports the validity of this new model. This study also accurately predicts the
110   gypsum deposition time on membrane material surfaces that is reported in the literature by
111   incorporating the deposition model our group developed previously. Using this new model with
112   solid theoretical basis, the gypsum scale management strategies can be optimized, such as recovery
113   rate, flow reversal frequencies, inhibitor dosages, to mention a few. Such optimizations can
114   significantly increase membrane operation efficiencies, drop the water desalination cost, and
115   promote the wider applications of membrane technologies, as well as other technologies wherein
116   gypsum formation is problematic.

117

2. Materials and Methods

2.1. Induction Time Testing

120   Reagent grade $CaCl_2 \cdot 2H_2O$, Na_2SO_4, and $NaCl$ salts were used to prepare solutions. The
121 cation (CAT) and anion solution (AN) solutions are prepared separately to include Ca^{2+} and SO_4^{2-}
122 ions at designed concentrations (Table S1), respectively. The saturation index of gypsum, defined
123 as the base ten (Briggsian) logarithms of the ion activity product over the solubility product, after
124 mixing the CAT and AN solutions with equal volume were calculated using *ScaleSoftPitzer* (*SSP*)
125 model (Dai et al., 2017a, 2014; Kan et al., 2015; Kan and Tomson, 2012), which is widely used as
126 one of most accurate thermodynamic models (Mavredaki et al., 2011). In Figure 1 is plotted the
127 multi-channel laser testing apparatus for induction time testing designed by Paudyal et al. (2020)
128 (Paudyal et al., 2020). This apparatus is modified from the single channel laser testing apparatus
129 used in previous research (C. Dai et al., 2019; Dai et al., 2017b; He et al., 1995a; Yan et al., 2015).
130 The customized heating block (Chemglass, CG-1991-03) has seven reaction vial (with a volume
131 of 30 mL) holders and seven tests can be conducted simultaneously. The laser light path was drilled
132 in the heating block with a cross-section view shown in Figure 1. CAT and AN solutions were
133 added at the same time into the reaction vial using two pipettes and the recording of induction time
134 was started. The heating and stirring is conducted by a digital hot plate stirrer (MR Hei-Tec).The
135 induction time is picked when the laser signal starts to drop by about 1%, which indicates the
136 formation of detectable minerals (Z. Dai et al., 2019). Various commonly used scale inhibitors
137 were added with different dosages in the AN solution to evaluate the inhibitor impacts. The tested
138 inhibitors are listed in Table 1 and their structures are plotted in Figure 2. The relative errors of
139 the induction time measurement are around 5%.

140
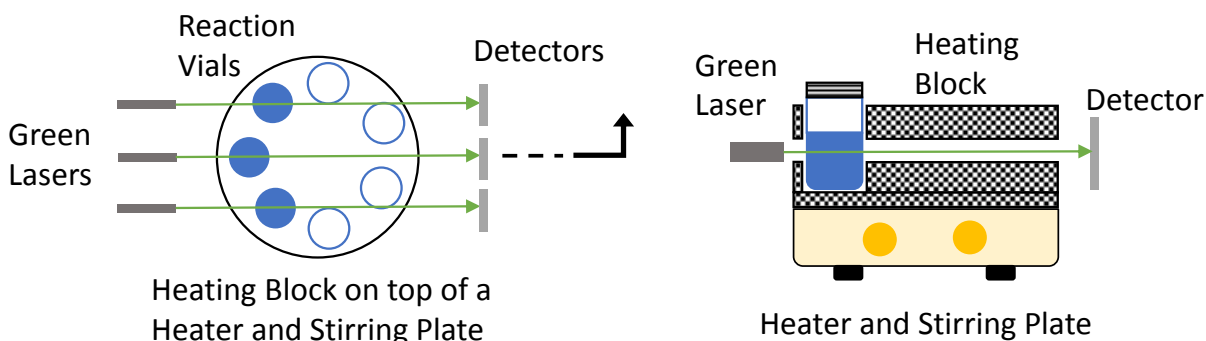
141
142 Figure 1. Top (left) and side (right) view of the schematic diagrams of the multi-channel laser
143 testing apparatus.

144

145   Table 1. Information of the inhibitors used in this study.

Short name	Full name	MW (g/mol)	number of Phosphonate group	number of Carboxylate group	number of Sulfonate group	MW per functional unit
BHPMP	bis-hexamethylene triamine-penta(methylene phosphonic) acid	685	5	0	0	137
DTPMP	diethylenetriamine-penta(methylene phosphonic) acid	573	5	0	0	115
HDTMP	hexamethylenediaminetetra(methylene phosphonic) acid	492	4	0	0	123
NTMP	nitrolotri(methylene phosphonic) acid	299	3	0	0	100
EDTMP	Ethylenediamine tetra (methylene phosphonic) acid	436	4	0	0	109
HEDP	1-hydroxyethylidene-1,1-diposphonic acid	206	2	0	0	103
PPCA	phosphinopolycarboxylic acid	3800	0	51	0	74.5
CMI	Carboxymethylinulin (25% substituted)	205.5*	0	0.75	0	274
PMAC	P-tagged Maleic acid polymer	116*	0	2	0	58
PVS	Polyvinyl sulfonate	107*	0	0	1	107

146   * Molecular weight of monomer is used since the molecular weight of the polymer is not available.

147

148

BHPMP DTPMP NTMP HDTMP EDTMP HEDP PPCA PVS CMI
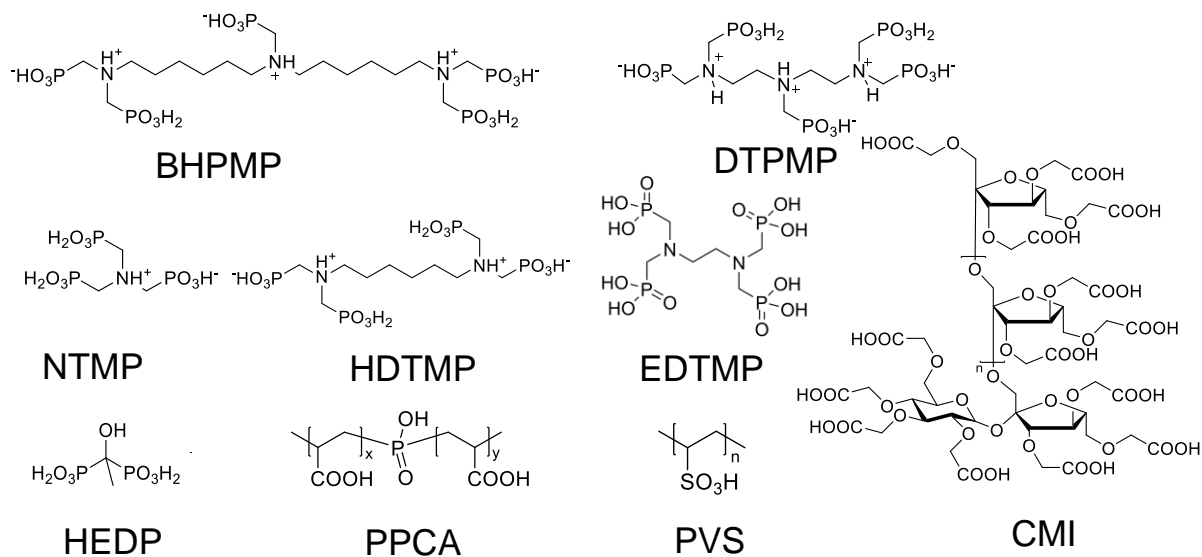
149
150   Figure 2. Structures of scale inhibitors.

151

152   Table 2. The experimental conditions of the precipitation and inhibition kinetics for gypsum.
153   Detailed information can be found in Table S1.

Inhibitors	Range of T (K)	Range of gypsum SI	Maximum inhibitor (mg/L active)	NaCl (mol/L)	# of data points
BHPMP	298 – 348	0.43 – 0.61	5	0.1 – 1	33
DTPMP	298 – 348	0.43 – 0.61	5	0.1 – 1	43
HDTMP	298 – 348	0.41 – 0.61	10	0.1 – 1	52
NTMP	298 – 298	0.56 – 0.76	20	3 – 3	10
EDTMP	298 – 298	0.56 – 0.56	2.5	3 – 3	4
HEDP	298 – 298	0.56 – 0.76	25	3 – 3	12
PPCA	298 – 348	0.43 – 0.76	20	0.1 – 3	56
CMI	298 – 298	0.56 – 0.76	25	3 – 3	13
PVS	298 – 298	0.56 – 0.56	15	3 – 3	7
No inhibitors	298 – 363	0.04 – 0.96	-	0 – 6	92

154

155   **2.2. Gypsum Crystallization and Inhibition Model Development**

156   The chemical reaction of gypsum crystallization and dissolution can be described as:

$$CaSO_4 \cdot 2H_2O \Longleftrightarrow Ca^{2+} + SO_4^{2-} + 2H_2O \tag{1}$$
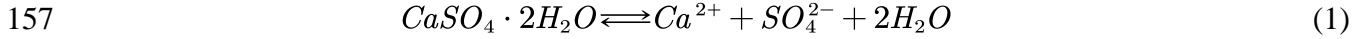
The saturation index of gypsum, SI, which is defined as the base ten logarithm of the ion activity product (IAP) over the solubility product: $SI_{gypsum} = \log_{10}(IAP/K_{sp,gypsum}) = \log_{10}(a_{Ca^{2+}}a_{SO_4^{2-}}a_{H_2O}^2/K_{sp})$. In this equation, a represents the activity of each species and equals to the product of the concentration (mol/kg H_2O, m) and activity coefficient (γ); K_{sp} is the gypsum solubility product. SI equals to 0 when the mineral is in equilibrium with the aqueous solution, positive when the mineral is supersaturated and has the potential to precipitate, and negative when the mineral is undersaturated. The SI values of each mineral and activity coefficient of each species at different conditions are calculated by the SSP model.

The supersaturation of minerals will lead to mineral crystallization with the decrease of Gibbs free energy and the increase of interfacial energy (Mullin, 2001). Söhnel and Mullin (1979, 1988) assumed that the mineral crystallization started with nucleation followed by polynuclear growth in the crystal growth stage, and the induction times were derived as follows (Nielsen, 1964; Söhnel and Mullin, 1988):

$$t_{ind} = \left(\frac{3}{2\pi}\right)^{1/4} \left(\frac{V_m^{5/3}}{A_v^{8/3} D^4 c_{eq}}\right)^{1/4} \left(\frac{10^{SI/2}}{(10^{SI/2}-1)^2}\right)^{1/4} \exp\left(\frac{\beta V_m^2 \sigma^3 A_v}{4(RT)^3 (2.303 \cdot SI)^2} + \frac{\beta' V_m^{4/3} \sigma^2 A_v^{2/3}}{4(RT)^2 (2.303 \cdot SI)}\right)$$

, $\tag{2}$

where R is the ideal gas constant (8.31 J K^{-1} mol^{-1}); T is temperature in Kelvin (K); V_m is the molar volume of mineral; σ is the superficial interfacial energy between mineral and solution (J m^{-2}); A_v is the Avogadro constant (6.02×10^{23} mol^{-1}); D is the effective diffusion coefficient (m^2 s^{-1}); c_{eq} is the equilibrium concentration of the lattice ions (mol m^{-3}) that can be calculated using *ScaleSoftPitzer*; β and β' are the shape factors (i.e., for spheres, $\beta = 16\pi/3$, $\beta' = \pi$); the first term in the exponential part is the contribution of nucleation and the second term is due to crystal growth. He et al. (1994a) found that the logarithm of the gypsum crystallization induction time does not follow a simple linear relationship with SI^{-2}, as suggested by CNT (He et al., 1994a). Such deviation from the CNT was proposed to be because gypsum has two different effective surface tensions, one for heterogeneous and one for homogenous nucleation (Mullin and Ang, 1976; Söhnel and Mullin, 1988, 1978). However, this assumption did not specify the transition SI value between these two types of nucleation and could lead to an abrupt change of induction time around the transition SI, which was inconsistent with the experimental observations.

In this study, it is assumed that the gypsum nucleation is dominated by the homogeneous nucleation when the SI is large (Huang et al., 2020; Lancia et al., 1999; Mullin, 2001). When the gypsum SI becomes smaller (i.e., less supersaturated), the nucleation process is gradually more dominated by heterogenous nucleation that may happen on the surface of impurities. Such transition can be represented by a gradual decrease of surface tension using the following sigmoid type of function:

$$193 \qquad \sigma = \sigma_0 \times (1 + \lambda_T T) \times \left(1 + \frac{a}{1 + e^{-b(SI-c)}}\right). \qquad (3)$$

194   where σ_0, a, b, and c are constants to be fitted; λ_T is the temperature dependence coefficient of
195   surface tension. It deserves notice that this sigmoid function is selected only to ensure a smooth
196   transition between the homogenous- and heterogenous-dominated nucleation. The calculated value
197   represents the superficial surface tension changing with the supersaturation of gypsum.

198   It is proposed that the scale inhibitors will adsorb onto the surface of gypsum nucleus and
199   thereby change the surface tension of the nucleus. This mechanism was assumed to be the
200   dominant mechanism in this model. The adsorption can be described by a Langmuir type
201   adsorption isotherm as follows:

$$202 \qquad q_e = \frac{q_m K_L [Inh]}{1 + K_L [Inh]} \qquad (4)$$

203   where q_e is the effective inhibitor concentration on the nucleus surface (mol/m^2 nucleus surface);
204   q_m is the maximum inhibitor concentration on the surface (mol/m^2 nucleus surface). Divide both
205   sides by q_m:

$$206 \qquad \theta = \frac{K_L [Inh]}{1 + K_L [Inh]} \qquad (5)$$

207   where $\theta = q_e/q_m$ and is the effective fraction coverage of the surface-active sites. The adsorption
208   of inhibitors onto the surface of gypsum nucleus can change the surface tension of gypsum nucleus
209   following a linear relationship proposed by Eberhart (1996) for a two components binary system
210   (Eberhart, 1966):

$$211 \qquad \sigma_{XY} = (1 - x_Y)\sigma_X + x_Y \sigma_Y \qquad (6)$$

212   where X and Y are the two components; x_Y is the mole fraction of component Y. For most cases,
213   the threshold scale inhibitors have a small molar ratio on the surface. For example, Zieba et al.
214   (1996) suggested that the effective active site coverage is less than 5% for phosphonate inhibitors
215   on gypsum and barite (Zieba et al., 1996). Tomson et al. (2003) found that NTMP
216   (nitrilomethylene phosphonic acid) occupies about 16% effective active sites of barite surface
217   (Tomson et al., 2003; Zieba et al., 1996). Thus, the surface tension of nuclei with inhibitor
218   adsorption can be estimated to be:

$$219 \qquad \sigma_{w/ Inh} \approx \sigma_X + x_{Inh} \sigma_{Inh} \qquad (7)$$

220   where σ_{Inh} is the surface tension of the inhibitor; x_{Inh} is proportional to the effective coverage
221   fraction θ as $x_{Inh} = B\theta$, where B is the molar ratio of the active sites over mineral molecule on the
222   nucleus surface. Thus, the surface tension of gypsum in the presence of inhibitors is:

$$223 \qquad \sigma_{w/ Inh} \approx \sigma_X + \frac{BK_L [Inh]}{1 + K_L [Inh]} \sigma_{Inh} = \sigma_X + \frac{(B\sigma_{Inh})K_L [Inh]}{1 + K_L [Inh]}. \qquad (8)$$

224   Considering that the total adsorbed amount of inhibitor is minimal comparing with the initial
225   total inhibitor concentration during the induction period, the equilibrium inhibitor concentration
226   (i.e., [Inh]) is estimated to be equal to the initial total inhibitor concentration. Via minimizing the
227   difference between the predicted and the measured induction time of all experiments (Table S1),

228   the SI dependent interfacial energy of gypsum, effective diffusion coefficient, interfacial energy
229   of the inhibitor, and the adsorption isotherms are optimized. The induction time of gypsum with
230   or without the presence of inhibitors can be calculated using the new mechanistic crystallization
231   and inhibition model by substituting Equation (8) in Equation (2).

232

3. Results and Discussions
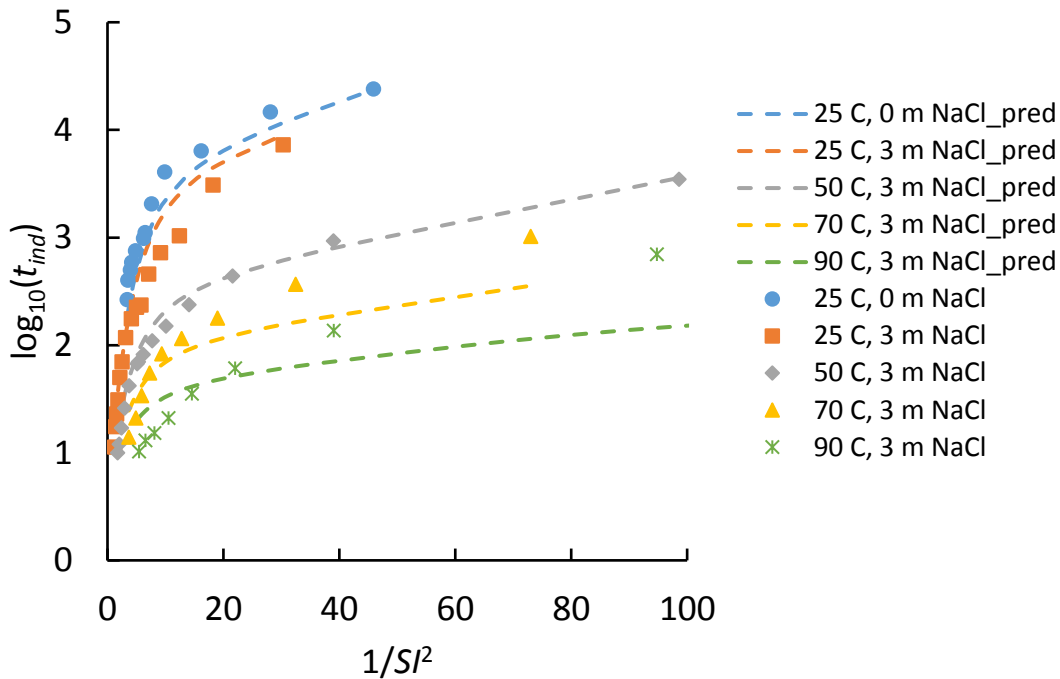
3.1. Induction Time of Gypsum Crystallization without Inhibitors

235   Based on Equation (2), the surface tension of gypsum depending on temperature and gypsum
236   *SI* is fitted to be $4.54E\text{-}4 \times (1 - 1.76E\text{-}3 \times T) \times [1 + 79.19 / (1 + \exp(-7.45 \times (SI - 0.125)))]$ J/m^2.
237   In Figure 3 is plotted the surface tension changes with *SI*, with the red box showing the gypsum *SI*
238   range of the experimental data in this study. It is shown the gypsum surface tension is about 17.26
239   mJ/m^2 at large gypsum *SI* values (e.g., > 1.1). At such high *SI* values, it is suggested that nucleation
240   is homogeneous. When *SI* value drops, the surface tension gradually decreases, with the inflection
241   point of *SI* around 0.125. At *SI* values above 0.48, the gypsum surface tension is above 90% of the
242   homogeneous surface tension. Such surface tension change indicates the gradual transition from
243   pure homogenous nucleation at large *SI* values to the co-occurrence of homogenous and
244   heterogeneous nucleation at relatively lower *SI* values. In previous research, it was proposed that
245   mineral deposition can be initiated by two pathways: (1) homogenous nucleation in the solution
246   followed by solids attachment to the surface, and (2) heterogeneous nucleation and crystallization
247   directly on the surface (Huang et al., 2020; Matin et al., 2019). The second path is believed to be
248   more energy favorable and happens at low *SI* values (Matin et al., 2019), which matches with what
249   has been observed in this study.
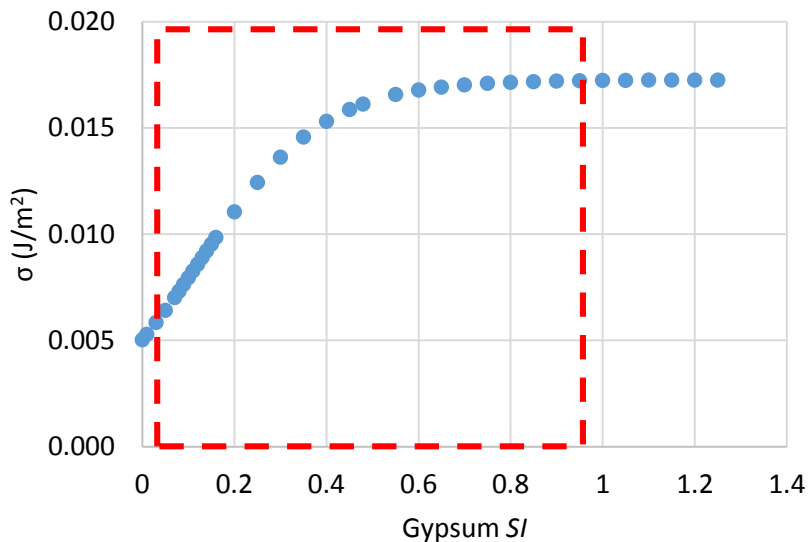
250
251   Figure 3. The surface tension of gypsum changes with *SI* at 25 °C, where the red box shows the
252   *SI* range of the experimental data. The X axis is the gypsum *SI*, and the Y axis is the surface
253   tension of gypsum.

255   In Figure 4 is plotted the induction time of gypsum without the presence of inhibitors
256 changing with SI^{-2} at different temperatures. The comparison between the measured and predicted
257 $\log_{10}(t_{ind})$ at all conditions are plotted in the first subplot of Figure 5. Note that $\log_{10}(t_{ind})$ does not
258 follow a linear relationship with SI^{-2} as predicted by CNT. The SI dependent surface tension fitted
259 above (Equation (3)) accurately explains such deviations from CNT. At higher temperatures, the
260 new model prediction shows a larger deviation, which might be due to potential phase change to
261 hemihydrate or anhydrite at higher temperatures (Blount and Dickson, 1973). It was reported that
262 the transition temperature between gypsum and anhydrite at 1 atm is around 40 °C and gypsum is
263 the dominant phase at temperatures below 40 °C (Lu et al., 2012; Rolnick, 1954).

264
265 Figure 4. The measured (symbols) and predicted (dotted lines) base ten logarithm of the gypsum
266 crystallization induction time at different temperatures and background salt concentrations,
267 without any inhibitors.
268
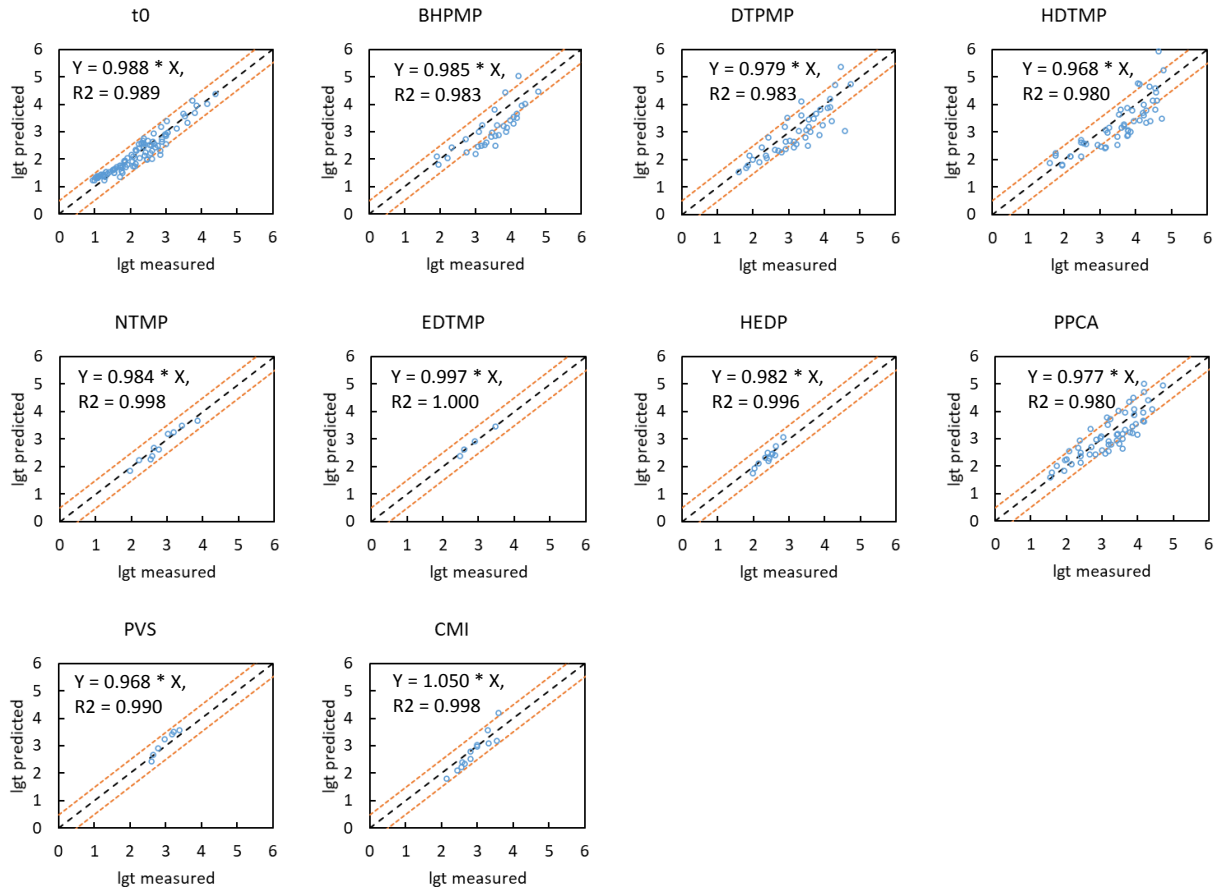
Figure 5. The predicted (Y axis) and measured (X axis) $\log_{10}(t_{ind})$ without or with nine different inhibitors at different conditions. The black dotted line is the 1:1 line and the red lines are the $\pm$ 0.5 error band. The linear correlation equations are also listed in each subplot.

3.2. Induction Time of Gypsum Crystallization with Inhibitors

In Figure 5 is plotted the comparison of the predicted and measured $\log_{10}(t_{ind})$ with the presence and absence of various inhibitors at different conditions (Table 2). The background ionic strength is picked to cover the extreme conditions that may occur during various industrial processes, e.g., heat exchange, concentration polarization in membrane systems, produced water production in the oil and gas production and geotherm energy exploitation. Most of the data lie along the 1:1 line within the $\pm$ 0.5 error band, indicating the accuracy of this model. Due to the relative large uncertainty of such induction time measurements, a $\pm$ 0.7 error band was used in previous research (Reznik et al., 2012). In Figure 6 and Figure 7 are plotted the specific examples showing the comparison between measured (symbols) and predicted (lines) $\log_{10}(t_{ind})$ of gypsum crystallization changing with inhibitor concentrations. It was observed that, different from that of the barite and calcite crystallization kinetics (C. Dai et al., 2019; Dai et al., 2020, 2017b; He et al., 1999, 1996, 1994b), the $\log_{10}(t_{ind})$ does not follow a linear relationship with the inhibitor concentration, especially when the inhibitor concentrations are large. Such non-linear correlations

make the empirical models proposed before (i.e., $log_{10}(t_{ind}) - log_{10}(t_{ind}^0) = b \cdot C_{in\square ibitor}$) inapplicable to the gypsum crystallization and inhibition kinetics predictions. The predicted induction times using this new model and the measured predicted induction times show good agreement, with a few exceptions. For some conditions for BHPMP, HDTMP, and PPCA, potentially due to experimental error (especially for those cases wherein the induction time is longer than 2 hours or more when large uncertainties exist) or the lack of temperature dependence of the inhibitor surface tension. Such agreement also validates the assumption that scale inhibitors prolong the induction time by adsorbing onto nucleus surface following a Langmuir type adsorption isotherm. The wide ranges of temperature, gypsum *SI* and background NaCl concentration give this model the potential to be widely applied to different industrial conditions. Furthermore once a single measurement of t_{ind} is made for any specific set of conditions and inhibitor concentration, calculation of the effect of changing any specific condition or concentration from the initially measured value is reliable, principally because this model is mechanistically based.
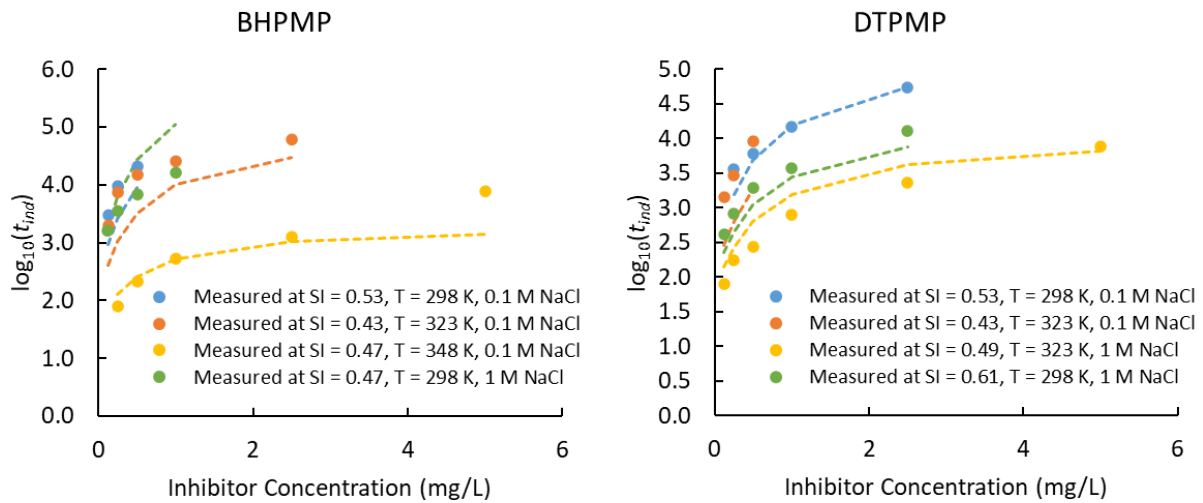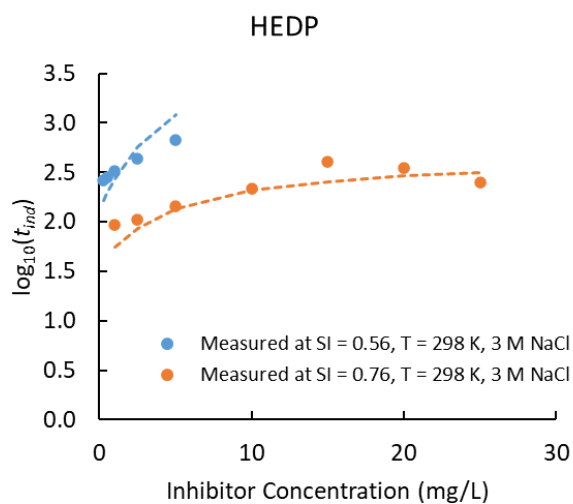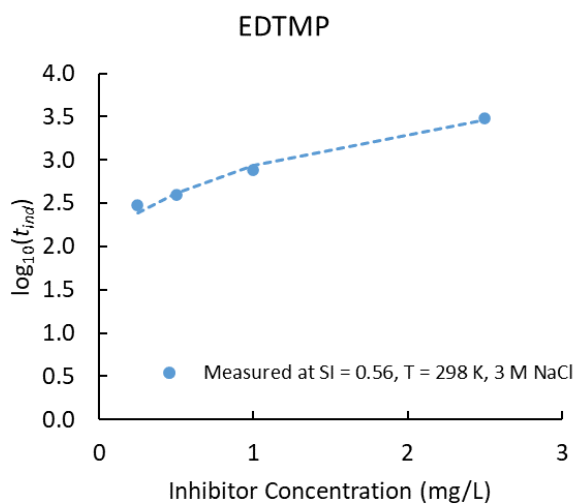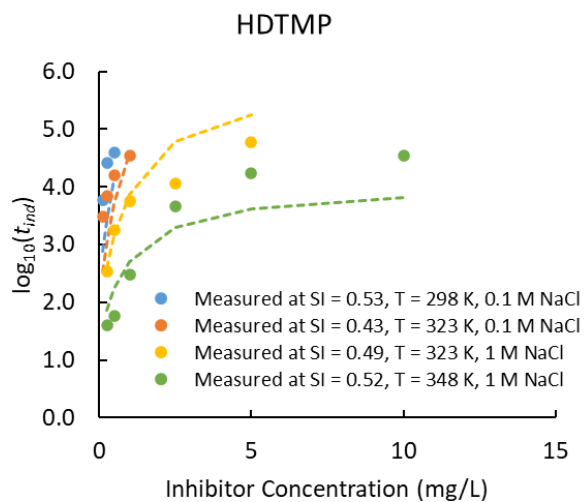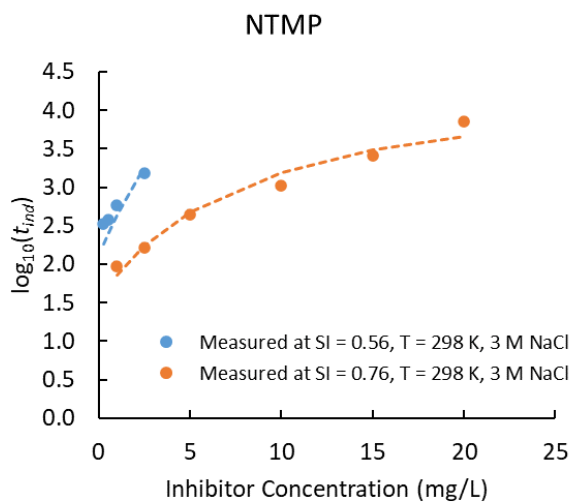
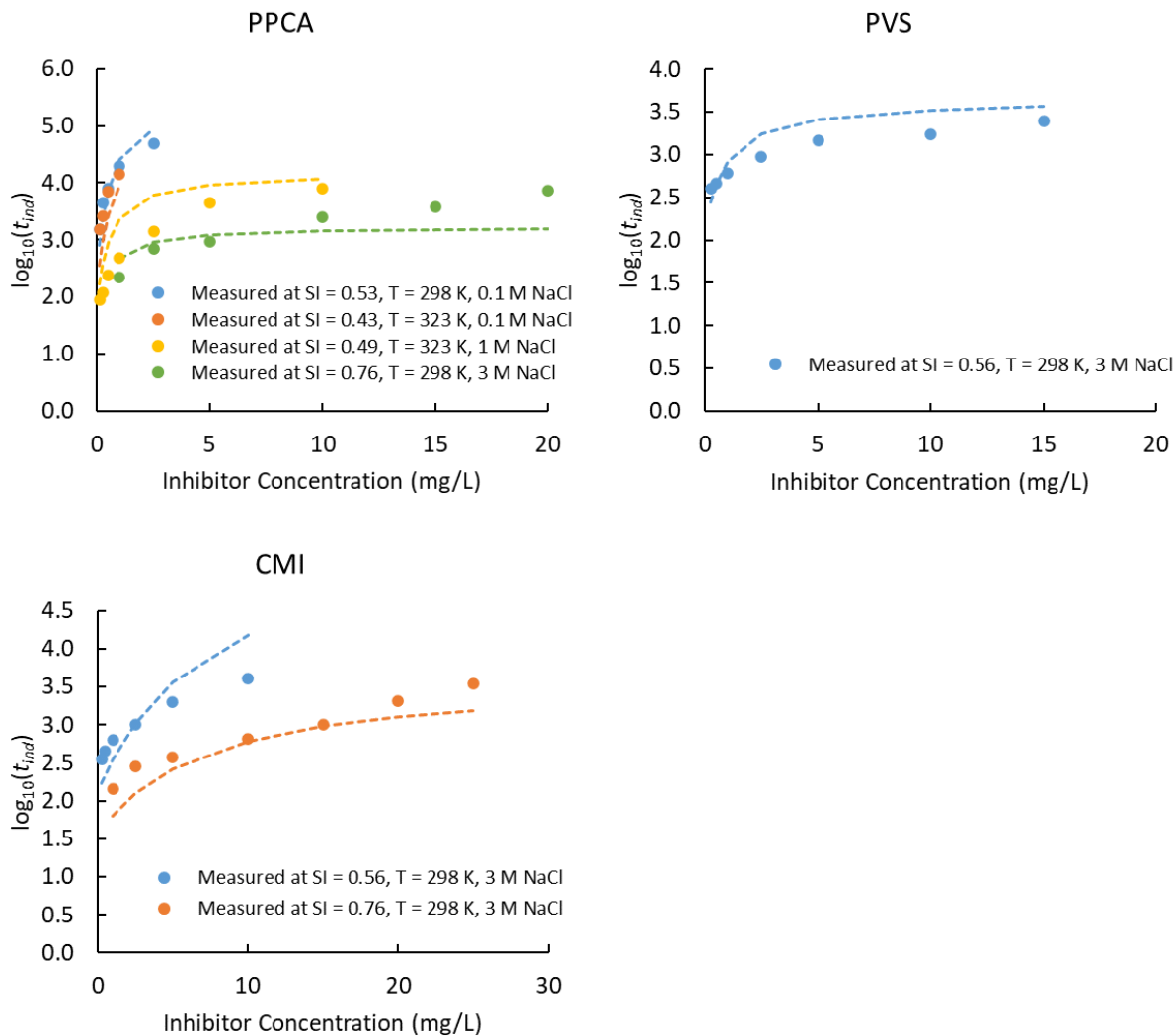Figure 6. $\log_{10}(t_{ind})$ of gypsum crystallization under various conditions changing with the concentrations of non-polymeric phosphonate inhibitors (i.e., BHPMP, DTPMP, HDTMP, NTMP, EDTMP, and HEDP). The symbols are experimental measurements, and the dotted lines are model predictions.

311

312

Figure 7. $\log_{10}(t_{ind})$ of gypsum crystallization under various conditions changing with the concentrations of polymeric inhibitors (i.e., PPCA, PVS, and CMI). The symbols are experimental measurements, and the dotted lines are model predictions.

3.3. Adsorption of Inhibitors on Gypsum

In Table 3 are listed the fitted $B\sigma_{Inh}$ and K_L values in Equation (8) of different inhibitors for gypsum crystallization from this study. The $B\sigma_{Inh}$ values indicate the maximum surface tension change if a large amount of scale inhibitor ($K_L[Inh] \gg 1$) were available. For example, at large inhibitor concentrations, HDTMP and NTMP show the largest surface tension change (i.e., most effective) of 117 and 120 mJ/m^2, respectively, while PVS shows the smallest surface tension change (i.e., least effective) of 51 mJ/m^2. The B term is the molar ratio of inhibitors over the mineral molecules on the nucleus surface, which was reported to be ranging from 5% (Zieba et al., 1996, p. 199) to 16% (Tomson et al., 2003) on different minerals and inhibitor types. Thus, the superficial surface tension of each inhibitor can be estimated by dividing the $B\sigma_{Inh}$ value with the

327 estimated B term value. The K_L values represent the affinity of inhibitors to the mineral nucleus.
328 When inhibitor concentration is $1/K_L$, the surface tension change is half of the maximum surface
329 tension change (i.e., 0.5 $B\sigma_{Inh}$). Thus, the inhibitors with smaller K_L values (e.g., CMI, NTMP, and
330 HEDP) have weaker affinity to the mineral surface and require larger inhibitor concentrations
331 (mol/L) to reach their maximum efficiency.
332   The K_L values between the inhibitors and celestite were fitted from the celestite
333 crystallization induction times and are listed in Table 3 (Zhao et al., 2022). It was observed that
334 the K_L values of the three inhibitors (i.e., DTPMP, PPCA, and PVS) with gypsum and celestite
335 follow a linear relationship with slope of 1.07 and R^2 of 0.9989. That implies that the inhibitors
336 with a strong affinity to gypsum usually represent a strong affinity to celestite as well. The K_L
337 values between the inhibitors and other minerals (i.e., barite, hydroxyapatite, and calcite) were also
338 calculated from crystal growth and dissolution rate changes. More studies to understand such
339 differences will be valuable.
340

Table 3. The fitted $B\sigma_{Inh}$ and K_L values of different inhibitors for gypsum crystallization from this study, and K_L values for different inhibitors on other minerals from literature.

		K_L (10^6 L/mol)							
		Gypsum	Celestite	Barite	Hydroxyapatite			Calcite	
Inhibitor	$B\sigma_{Inh}$ (mJ/m²)	This Study	Zhao et al. (2022)	Pina et al. (2004)	Zieba et al. (1996)	Amjad (1987)	Koutsoukos et al. (1981)	Sawada et al. (2003)	Reddy and Nancollas (1973)
BHPMP	8.1	1.45			1.7				
DTPMP	7.9	0.57	0.5		5.9				
HDTMP	11.7	0.61			1.3	1.40			
NTMP	12.0	0.03			1.2	0.62			
EDTMP	7.0	0.24			8.5	1.80		10.5	10.0
HEDP	6.1	0.03		0.22	1.9	1.33	2.08		
PPCA	8.2	4.02	4.3						
CMI	9.5	0.03							
PVS	5.1	0.10	0.2						

3.4. Applications in Membrane System Management

This new model, by substituting Equation (8) in Equation (2), can be used in understanding the gypsum crystallization and deposition (or fouling). For example, Huang et al. (2020) studied the impacts of surface hydrophobicity on gypsum deposition (Huang et al., 2020). They ran the testing at two different conditions (Table 4) to represent the homogeneous nucleation pathway at a higher SI (Condition 1) and the heterogeneous nucleation pathway at a smaller SI (Condition 2), respectively. Under Condition 1, the predicted induction time and the two measured induction times are probably within experimental error. In addition, under this condition, the surface tension is more than 90% of the homogenous nucleation surface tension (Equation (3)), indicating that homogeneous nucleation will be dominated, which matched reasonably well with their experimental results. Under Condition 2, the predicted induction time matched well with the induction times measured by He et al. (1996) and Huang et al. (2020). Different than Condition 1, Huang et al. (2020) believed that under Condition 2 heterogeneous nucleation is dominated and thus they used QCM-D (quartz crystal microbalance with dissipation) to monitor the deposition onto membrane material surfaces, instead of using DLS (dynamic light scattering) to monitor bulk crystallization. According to the mineral crystallization surface deposition platform our group developed (Dai et al., 2021; Lu et al., 2020a, 2020b, 2019), it is believed that the first phase deposition happens in the stagnant laminar sublayer following the same bulk crystallization kinetics. The good agreement between the detection of surface deposition by Huang et al. (2020) with the bulk crystallization induction time measured by He et al. (1994a) and predicted by this study further confirms the validity of the gypsum crystallization model proposed in this study and the mineral crystallization surface deposition platform proposed previously (Dai et al., 2021).

Table 4. Two gypsum crystallization conditions in Huang et al. (2020) and the comparison of the induction times by this study, He et al. (1994a) and Huang et al. (2020).

Experimental Conditions	$\log_{10}(t_{ind})$		
	This study	He et al. (1994a)	Signal change in Huang et al. (2020)
1: Na^+, Cl^-, Ca^{2+}, and SO_4^{2-} concentrations are 0.1, 0.1, 0.05, and 0.05 mol/L, $T = 22$ ºC, $SI = 0.51$ (SSP) and 0.52 (Visual Minteq)	2.50	2.70 ($SI = 0.50$, $T = 25$ ºC)	3.32 (35 min) (DLS)
2: Na^+, Cl^-, Ca^{2+}, and SO_4^{2-} concentrations are 0.05, 0.05, 0.025, and 0.025 mol/L, T = 22 ºC, $SI = 0.15$ (SSP) and 0.15 (Visual Minteq)	4.52	4.38 ($SI = 0.15$, $T = 25$ ºC)	4.55 (~ 10 hours) (QCM-D)

The utility of having this complete crystallization and inhibition model is apparent: in addition to predicting the initial induction times, the impact on crystallization by varying the conditions (temperature, saturation index, etc.) or addition of small amounts of threshold inhibitor

374 can readily be calculated. For example, under Condition 1, the addition of 1 mg/L of PPCA can
375 prolong the induction time to about 17.5 hours (i.e., $10^{4.80}$ seconds). That means, in a membrane
376 water treatment system, the addition of 1 mg/L of PPCA in the concentrate side can significantly
377 reduce the periodical feed water flush frequency by a factor of 30 times if keeping the same
378 recovery ratio.
379

4. Conclusions

381 The unexpected mineral scale deposition and fouling in the membrane system has been one
382 of the main reasons that limit the wide applications of membrane treatment technology. However,
383 few mechanistic models are available to accurately predict the induction time of gypsum, one of
384 the most common and troublesome scale minerals. This study developed a new crystallization and
385 inhibition model based on the classical nucleation theory. This model assumes that the gypsum
386 surface tension is dependent on *SI*. At more supersaturated conditions, the surface tension is larger,
387 and is homogeneous nucleation dominated; at less saturated conditions, the surface tension
388 gradually decreases with more occurrences of heterogeneous nucleation. A sigmoid function is
389 used to describe such gradual transition from homogenous to heterogeneous nucleation. This
390 model accurately predicts the gypsum crystallization induction time at conditions of *SI* from 0.04
391 to 0.96, temperature from 25 to 90 ^{o}C, background NaCl salt concentration from 0 to 6 mol/L.
392 A Langmuir-type adsorption isotherm is adopted to describe the adsorption of inhibitors to
393 the gypsum nucleus surface. The surface tension of the gypsum nucleus will increase due to the
394 inhibitor adsorption. This study used this new model and accurately predicted the induction time
395 of gypsum crystallization in the presence and absence of nine commonly used scale inhibitors. The
396 fitted affinity constants (K_L) between these inhibitors and gypsum shows a good linear relationship
397 with those between the same inhibitors and barite, implying a similar adsorption mechanism.
398 This study successfully adopts the new crystallization model and resolves the long-unsolved
399 problem of gypsum crystallization kinetics prediction with or without the dosage of various scale
400 inhibitors. By incorporating the mineral surface deposition model developed before, this model
401 can accurately predict the deposition time of gypsum on the membrane material surface. The utility
402 of this model can help accurately evaluate the impacts of temperature, saturation index, and scale
403 inhibitors. Such predictions can help improve the operational efficiency of membrane systems,
404 including product water recovery, periodical feed water flush frequency, scale inhibitor type and
405 dosages at different operating conditions, to mention a few.
406

5. Acknowledgement

6. References

Alimi, F., Elfil, H., Gadri, A., 2003. Kinetics of the precipitation of calcium sulfate dihydrate in a desalination unit. Desalination, Desalination and the Environment: Fresh Water for All 158, 9–16. https://doi.org/10.1016/S0011-9164(03)00426-0

Al-Roomi, Y.M., Hussain, K.F., 2016. Potential kinetic model for scaling and scale inhibition mechanism. Desalination, Fouling and Scaling in Desalination 393, 186–195. https://doi.org/10.1016/j.desal.2015.07.025

Antony, A., Low, J.H., Gray, S., Childress, A.E., Le-Clech, P., Leslie, G., 2011. Scale formation and control in high pressure membrane water treatment systems: a review. J. Membr. Sci. 383, 1–16.

Blount, C.W., Dickson, F.W., 1973. Gypsum-anhydrite equilibria in systems CaSO4-H2O and CaCO4-NaCl-H2O. Am. Mineral. 58, 323–331.

Dai, C., Dai, Z., Zhang, F., Zhao, Y., Deng, G., Harouaka, K., Wang, X., Lu, Y.-T., Paudyal, S., Ko, S., 2019. A Unified Experimental Method and Model for Predicting Scale Inhibition. Presented at the SPE International Conference on Oilfield Chemistry, Society of Petroleum Engineers.

Dai, Z. (Joey), Lu, Y.-T., Kan, A., Leschied, C., Zhao, Y., Dai, C., Wang, X., Paudyal, S., Ko, S., Tomson, M., 2021. A mechanistic software platform for mineral surface deposition and inhibition prediction under different flow conditions. Desalination 509, 115071. https://doi.org/10.1016/j.desal.2021.115071

Dai, Z., Kan, A., Zhang, F., Tomson, M., 2014. A Thermodynamic Model for the Solubility Prediction of Barite, Calcite, Gypsum, and Anhydrite, and the Association Constant Estimation of CaSO4$^{(0)}$ Ion Pair up to 250 °C and 22000 psi. J. Chem. Eng. Data 60, 766–774. https://doi.org/10.1021/je5008873

Dai, Z., Kan, A.T., Shi, W., Zhang, N., Zhang, F., Yan, F., Bhandari, N., Zhang, Z., Liu, Y., Ruan, G., Tomson, M.B., 2017a. Solubility measurements and predictions of gypsum, anhydrite, and calcite over wide ranges of temperature, pressure, and ionic strength with mixed electrolytes. Rock Mech. Rock Eng. 50, 327–339. https://doi.org/10.1007/s00603-016-1123-9

Dai, Z., Li, Y., 2013. A multistage irrigation water allocation model for agricultural land-use planning under uncertainty. Agric. Water Manag. 129, 69–79.

Dai, Z., Zhang, F., Bhandari, N., Deng, G., Kan, A.T., Ruan, G., Yan, F., Zhang, Z., Liu, Y., Lu, A.Y., Tomson, M.B., 2017b. Development and application of a new theoretical model for additive impacts on mineral crystallization. Cryst. Growth Des. 17, 9. https://doi.org/10.1021/acs.cgd.7b00658

Dai, Z., Zhang, F., Kan, A.T., Ruan, G., Yan, F., Bhandari, N., Zhang, Z., Liu, Y., Lu, A.Y.-T., Deng, G., Tomson, M.B., 2019. Two-Stage Model Reveals Barite Crystallization Kinetics from Solution Turbidity. Ind. Eng. Chem. Res. 58, 10864–10874. https://doi.org/10.1021/acs.iecr.9b01707

Dai, Z., Zhang, F., Zhao, Y., Dai, C., Wang, X., Paudyal, S., Ko, S., Leschied, C., Yao, X., Kan, A.T., Tomson, M., 2020. Predicting Calcite Crystallization and Inhibition Kinetics at up to 175 °C Using a New Theoretical Inhibition Model. Cryst. Growth Des. 20, 8090–8100. https://doi.org/10.1021/acs.cgd.0c01381

Eberhart, J.G., 1966. The surface tension of binary liquid Mixtures. J. Phys. Chem. 70, 1183–1186.

Ghaffour, N., Missimer, T.M., Amy, G.L., 2013. Technical review and evaluation of the

461   economics of water desalination: Current and future challenges for better water supply
462   sustainability. Desalination 309, 197–207. https://doi.org/10.1016/j.desal.2012.10.015
463 Gryta, M., 2009. Calcium sulphate scaling in membrane distillation process. Chem. Pap. 63,
464   146–151.
465 He, S., Kan, A.T., Tomson, M.B., 1999. Inhibition of calcium carbonate precipitation in NaCl
466   brines from 25 to 90 °C. Appl. Geochem. 14, 17–25.
467 He, S., Kan, A.T., Tomson, M.B., 1996. Mathematical inhibitor model for barium sulfate scale
468   control. Langmuir 12, 1901–1905. https://doi.org/10.1021/La950876x
469 He, S., Oddo, J.E., Tomson, M.B., 1995a. The nucleation kinetics of barium sulfate in NaCl
470   solutions up to 6 m and 90 °C. J. Colloid Interface Sci. 174, 319–326.
471 He, S., Oddo, J.E., Tomson, M.B., 1995b. The Nucleation kinetics of strontium sulfate in NaCl
472   solutions up to 6 m and 90 C with or without inhibitors. J. Colloid Interface Sci. 174,
473   327–335.
474 He, S., Oddo, J.E., Tomson, M.B., 1994a. The Nucleation Kinetics of Calcium Sulfate Dihydrate
475   in NaCl Solutions up to 6 m and 90°C. J. Colloid Interface Sci. 162, 297–303.
476   https://doi.org/10.1006/jcis.1994.1042
477 He, S., Oddo, J.E., Tomson, M.B., 1994b. The inhibition of gypsum and barite nucleation in
478   NaCl brines at temperatures from 25 to 90 °C. Appl. Geochem. 9, 561–567.
479   https://doi.org/10.1016/0883-2927(94)90018-3
480 Huang, X., Li, C., Zuo, K., Li, Q., 2020. Predominant Effect of Material Surface Hydrophobicity
481   on Gypsum Scale Formation. Environ. Sci. Technol. 54, 15395–15404.
482   https://doi.org/10.1021/acs.est.0c03826
483 Kan, A.T., Dai, Z., Zhang, F., Bhandari, N., Yan, F., Zhang, Z., Liu, Y., Tomson, M.B., 2015.
484   Scale prediction and control at ultra HTHP. Presented at the SPE International
485   Symposium on Oilfield Chemistry, Society of Petroleum Engineers.
486 Kan, A.T., Tomson, M.B., 2012. Scale prediction for oil and gas production. SPE J. 17, 362–378.
487 Kelle Zeiher, E.H., Ho, B., Williams, K.D., 2003. Novel antiscalant dosing control. Desalination,
488   Desalination and the Environment: Fresh Water for all 157, 209–216.
489   https://doi.org/10.1016/S0011-9164(03)00400-4
490 Knezic, D., Zaccaro, J., Myerson, A.S., 2004. Nucleation induction time in levitated droplets. J.
491   Phys. Chem. B 108, 10672–10677. https://doi.org/10.1021/Jp049586s
492 Lancia, A., Musmarra, D., Prisciandaro, M., 1999. Measuring induction period for calcium
493   sulfate dihydrate precipitation. AIChE J. 45, 390–397.
494   https://doi.org/10.1002/aic.690450218
495 Lee, J.-G., Jang, Y., Fortunato, L., Jeong, S., Lee, S., Leiknes, T., Ghaffour, N., 2018. An
496   advanced online monitoring approach to study the scaling behavior in direct contact
497   membrane distillation. J. Membr. Sci. 546, 50–60.
498   https://doi.org/10.1016/j.memsci.2017.10.009
499 Lin, C.-J., Shirazi, S., Rao, P., 2005. Mechanistic Model for CaS O4 Fouling on Nanofiltration
500   Membrane. J. Environ. Eng. 131, 1387–1392. https://doi.org/10.1061/(ASCE)0733-
501   9372(2005)131:10(1387)
502 Lin, Y.-P., Singer, P.C., 2005. Inhibition of calcite crystal growth by polyphosphates. Water Res.
503   39, 4835–4843. https://doi.org/10.1016/j.watres.2005.10.003
504 Lioliou, M.G., Paraskeva, C.A., Koutsoukos, P.G., Payatakes, A.C., 2006. Calcium sulfate
505   precipitation in the presence of water-soluble polymers. J. Colloid Interface Sci. 303,
506   164–170. https://doi.org/10.1016/j.jcis.2006.07.054

Lu, A.Y.-T., Harouaka, K., Paudyal, S., Ko, S., Dai, C., Gao, S., Deng, G., Zhao, Y., Wang, X., Mateen, S., 2020a. Kinetics of Barium Sulfate Deposition and Crystallization Process in the Flowing Tube. Ind. Eng. Chem. Res. 59, 7299–7309.

Lu, A.Y.-T., Paudyal, S., Ko, S., Dai, C., Ouyang, B., Deng, G., Zhao, Y., Wang, X., Mateen, S., Liu, H., 2020b. Does Barite Scale Deposit at a Kinetic Stable Flow?, in: SPE Virtual International Oilfield Scale Conference and Exhibition. Society of Petroleum Engineers.

Lu, A.Y.-T., Shi, W., Wang, J., Venkatesan, R., Harouaka, K., Paudyal, S., Ko, S., Dai, C., Gao, S., Deng, G., 2019. The Mechanism of Barium Sulfate Deposition Inhibition and the Prediction of Inhibitor Dosage. J. Chem. Eng. Data 64, 4968–4976.

Lu, H.P., Kan, A.T., Zhang, P., Yu, J., Fan, C.F., Work, S., Tomson, M.B., 2012. Phase Stability and Inhibition of Calcium Sulfate in the System NaCl/Monoethylene Glycol/H2O. Spe J. 17, 187–197.

Matin, A., Rahman, F., Shafi, H.Z., Zubair, S.M., 2019. Scaling of reverse osmosis membranes used in water desalination: Phenomena, impact, and control; future directions. Desalination 455, 135–157. https://doi.org/10.1016/j.desal.2018.12.009

Mavredaki, E., Neville, A., Sorbie, K.S., 2011. Initial stages of barium sulfate formation at surfaces in the presence of inhibitors. Cryst. Growth Des. 11, 4751–4758. https://doi.org/10.1021/cg101584f

Mukhopadhyay, D., 2003. Method and apparatus for high efficiency reverse osmosis operation. US6537456B2.

Mullin, J.W., 2001. Crystallization. Butterworth-Heinemann.

Mullin, J.W., Ang, H.M., 1976. Nucleation characteristics of aqueous nickel ammonium sulphate solutions. Faraday Discuss. Chem. Soc. 61, 141–148.

Nghiem, L.D., Cath, T., 2011. A scaling mitigation approach during direct contact membrane distillation. Sep. Purif. Technol. 80, 315–322. https://doi.org/10.1016/j.seppur.2011.05.013

Nielsen, A.E., 1964. Kinetics of precipitation. Pergamon Press Oxford.

Paudyal, S., Mateen, S., Dai, C., Ko, S., Wang, X., Deng, G., Lu, A., Zhao, Y., Bingjie, O., Kan, A.T., Tomson, M.B., 2020. Developments on Calcium Sulfate Scaling Prediction and Control in Oil and Gas Production. Presented at the SPE International Oilfield Scale Conference and Exhibition, OnePetro. https://doi.org/10.2118/200671-MS

Pomerantz, N., Ladizhansky, Y., Korin, E., Waisman, M., Daltrophe, N., Gilron, J., 2006. Prevention of Scaling of Reverse Osmosis Membranes by "Zeroing" the Elapsed Nucleation Time. Part I. Calcium Sulfate. Ind. Eng. Chem. Res. 45, 2008–2016. https://doi.org/10.1021/ie051040k

Prisciandaro, M., Olivieri, E., Lancia, A., Musmarra, D., 2006. Gypsum Precipitation from an Aqueous Solution in the Presence of Nitrilotrimethylenephosphonic Acid. Ind. Eng. Chem. Res. 45, 2070–2076. https://doi.org/10.1021/ie050615a

Rabie, H.R., Côté, P., Adams, N., 2001. A method for assessing membrane fouling in pilot- and full-scale systems. Desalination 141, 237–243. https://doi.org/10.1016/S0011-9164(01)85002-5

Reznik, I.J., Ganor, J., Gruber, C., Gavrieli, I., 2012. Towards the establishment of a general rate law for gypsum nucleation. Geochim. Cosmochim. Acta 85, 75–87. https://doi.org/10.1016/j.gca.2012.02.002

Rolnick, L.S., 1954. The stability of gypsum and anhydrite in the geologic environment. Massachusetts Institute of Technology.

553   Rosenberg, Y.O., Reznik, I.J., Zmora-Nahum, S., Ganor, J., 2012. The effect of pH on the
554   formation of a gypsum scale in the presence of a phosphonate antiscalant. Desalination
555   284, 207–220. https://doi.org/10.1016/j.desal.2011.08.061
556   Seidel, A., Elimelech, M., 2002. Coupling between chemical and physical interactions in natural
557   organic matter (NOM) fouling of nanofiltration membranes: implications for fouling
558   control. J. Membr. Sci. 203, 245–255. https://doi.org/10.1016/S0376-7388(02)00013-3
559   Shirazi, S., Lin, C.-J., Chen, D., 2010. Inorganic fouling of pressure-driven membrane processes
560   — A critical review. Desalination 250, 236–248.
561   https://doi.org/10.1016/j.desal.2009.02.056
562   Söhnel, O., Mullin, J.W., 1988. Interpretation of crystallization induction periods. J. Colloid
563   Interface Sci. 123, 43–50.
564   Söhnel, O., Mullin, J.W., 1978. A method for the determination of precipitation induction
565   periods. J. Cryst. Growth 44, 377–382.
566   Speth, T.F., Summers, R.S., Gusses, A.M., 1998. Nanofiltration Foulants from a Treated Surface
567   Water. Environ. Sci. Technol. 32, 3612–3617. https://doi.org/10.1021/es9800434
568   Tomson, M., Fu, G., Watson, M., Kan, A., 2003. Mechanisms of mineral scale inhibition. SPE
569   Prod. Facil. 18, 192–199.
570   Uchymiak, M., Bartman, A.R., Daltrophe, N., Weissman, M., Gilron, J., Christofides, P.D.,
571   Kaiser, W.J., Cohen, Y., 2009. Brackish water reverse osmosis (BWRO) operation in
572   feed flow reversal mode using an ex situ scale observation detector (EXSOD). J. Membr.
573   Sci. 341, 60–66. https://doi.org/10.1016/j.memsci.2009.05.039
574   Van der Bruggen, B., Everaert, K., Wilms, D., Vandecasteele, C., 2001. The use of nanofiltration
575   for the removal of pesticides from groundwater: an evaluation. Water Supply 1, 99–106.
576   https://doi.org/10.2166/ws.2001.0026
577   Van der Leeden, M., Kashchiev, D., Van Rosmalen, G., 1992. Precipitation of barium sulfate:
578   Induction time and the effect of an additive on nucleation and growth. J. Colloid Interface
579   Sci. 152, 338–350.
580   Warsinger, D.M., Swaminathan, J., Guillen-Burrieza, E., Arafat, H.A., Lienhard V, J.H., 2015.
581   Scaling and fouling in membrane distillation for desalination applications: A review.
582   Desalination, State-of-the-Art Reviews in Desalination 356, 294–313.
583   https://doi.org/10.1016/j.desal.2014.06.031
584   Yan, C., Kan, A.T., Zhang, F., Liu, Y., Tomson, R.C., Tomson, M.B., 2015. Systematic study of
585   barite nucleation and inhibition with various polymeric scale inhibitors by novel laser
586   apparatus. SPE J. 20, 642–651.
587   Yu, W., Song, D., Li, A., Yang, H., 2019. Control of gypsum-dominated scaling in reverse
588   osmosis system using carboxymethyl cellulose. J. Membr. Sci. 577, 20–30.
589   https://doi.org/10.1016/j.memsci.2019.01.053
590   Zhang, F., Dai, Z., Yan, C., Bhandari, N., Yan, F., Liu, Y., Zhang, Z., Ruan, G., Kan, A.T.,
591   Tomson, M.B., 2017. Barite-Scaling Risk and Inhibition at High Temperature. SPE J. 22,
592   69–79. https://doi.org/10.2118/169771-PA
593   Zhao, Y., Dai, Z., Wang, X., Dai, C., Paudyal, S., Ko, S., Kan, A.T., Tomson, M., 2022. A New
594   Mechanistic Model for Mineral Crystallization and Inhibition Kinetics and Its
595   Application to Celestite. SPE J.
596   Zieba, A., Sethuraman, G., Perez, F., Nancollas, G.H., Cameron, D., 1996. Influence of organic
597   phosphonates on hydroxyapatite crystal growth kinetics. Langmuir 12, 2853–2858.
598   Zuo, K., Kim, J., Jain, A., Wang, T., Verduzco, R., Long, M., Li, Q., 2018. Novel Composite

599   Electrodes for Selective Removal of Sulfate by the Capacitive Deionization Process.
600   Environ. Sci. Technol. 52, 9486–9494. https://doi.org/10.1021/acs.est.8b01868
601

Click here to access/download
Electronic Supplementary Material (for online publication only)
Supporting Information.docx